Check for updates

The study of thermodynamic mechanisms of advection-cooled sea fogs for two cases based on the WRF model

Xin-Ya Ye[1], Fei-Fei Shen[1,2,3]*, Hai-Yan Fei[4], Qi-Long Sun[5], Ai-Qing Shu[1], Shen Wan[1] and He Chen[1]

[1]Key Laboratory of Meteorological Disaster, Ministry of Education/Joint International Research Laboratory of Climate and Environment Change/Collaborative Innovation Center on Forecast and Evaluation of Meteorological Disasters, Nanjing University of Information Science and Technology, Nanjing, Jiangsu, China, [2]East China Phased Array Weather Radar Application Joint Laboratory, Shanghai, China, [3]China Meteorological Administration Tornado Key Laboratory, Guangzhou, China, [4]China Meteorological Administration Training Centre, Beijing, China, [5]Chongqing Institute of Green and Intelligent Technology, Chinese Academy of Sciences, Chongqing, China

Introduction: Sea fog significantly affects maritime transportation and coastal safety. This study investigates the thermodynamic mechanisms driving two persistent sea fog events in China: one along the coast of Zhejiang Province (March 27–April 2, 2018) and another in the Qiongzhou Strait (January 20–26, 2021). Although both events are primarily caused by advection cooling, their underlying thermodynamic structures differ due to varying synoptic and mesoscale conditions.

Methods: High-resolution numerical simulations were performed using the Weather Research and Forecasting (WRF) model. Supplementary data sources include MICAPS surface observations, ERA reanalysis data, and radiance measurements from the FY-4A satellite. A combination of synoptic background analysis, mesoscale structural examination, and thermodynamic field diagnostics was used to identify the mechanisms of fog formation. The accuracy of fog extent prediction was also evaluated using the FSL (based on relative humidity) and SW99 (based on cloud-water mixing ratio) visibility algorithms.

Results: Both fog events were driven by advection cooling but exhibited distinct thermodynamic profiles. The Zhejiang case was characterized by warm and moist advection over a cold sea surface, with a pronounced sea-air temperature gradient, a low inversion layer (below 850 hPa), and moderate atmospheric stability. The Qiongzhou Strait case showed a deeper and more stable atmospheric structure, with warm advection extending down to 950 hPa and a discontinuous inversion layer at higher levels, contributing to greater thermodynamic stability. In terms of fog prediction, the FSL algorithm outperformed SW99 in estimating fog coverage, although both had limitations in accurately predicting visibility levels.

Discussion: This comparative analysis highlights the influence of differing synoptic and mesoscale conditions on the formation and evolution of advection-cooled sea fog. The results suggest that regional fog forecasting

can benefit from a synergistic thermodynamic-dynamic diagnostic framework. Understanding these differences enhances the ability to forecast fog development under varying meteorological backgrounds.

1 Introduction

Sea fogs refer to a weather phenomenon in which water droplets or ice crystals condense in the lower atmosphere over coastal areas or the sea, resulting in horizontal visibility of less than 1 km. With its long coastline, China experiences persistent sea fog events annually from February to August, particularly along the coasts of Fujian, the Bohai Sea, and the Yellow Sea, exhibiting distinct seasonal characteristics. The occurrence of sea fog disrupts maritime navigation, fishing activities, and the daily lives of coastal residents (Bergot and Koracin, 2021). However, due to the complex microphysical mechanisms involved, accurate and refined forecasting of sea fog remains a significant challenge.

The main types of sea fogs in China's coastal waters are advection fog and radiation fog (Liang and Griswold, 2024). Advection fog is more common in spring and summer, formed when warm and humid air moves over a colder sea surface. Radiation fog typically forms during the autumn and winter, primarily at night or in the early morning, as air near the surface cools due to radiative cooling (Yang et al., 2024). Once sea fog forms, long-wave radiation cooling at the fog top induces turbulent mixing, which further promotes water vapor condensation. Therefore, turbulence plays a crucial role in the development of sea fog (Meng et al., 2025).

Many studies have investigated typical sea fog cases in various regions, analyzing the dominant mechanisms of sea fog formation and the physical factors influencing its development (Yun and Ha, 2022; Zhang et al., 2009; Han and Long, 2022; Liang et al., 2009; Tian et al., 2019; Wang et al., 2014; Niu, F. et al., 2010). Observing sea fog is particularly challenging due to the shallow nature of the fog layer, its rapid spatial changes, and the difficulty in measuring microphysical parameters such as water droplet size and concentration. Lee et al. (2021) studied the mechanism of a sea fog event in the Yellow Sea, and pointed out that the nighttime warm air advection and cooling process promoted the formation and intensification of sea fog, while the daytime shortwave radiation heating and dry air advection led to the dissipation of fog. According to Gultepe et al. (2017), sea fog formation is primarily influenced by water vapor transport, longwave radiative cooling at the fog top, and turbulent mixing in the boundary layer. These processes affect the liquid water content (LWC) and droplet concentration, which are crucial for fog persistence and visibility.

Given the challenges in observing sea fog, numerical simulations have become an essential tool for understanding and predicting its high spatial and temporal variability. Numerical Weather Prediction (NWP) models, such as the Weather Research and Forecasting Model (WRF), have been widely used to simulate the physical processes that govern sea fog formation, including turbulence, radiation, and surface coupling (Lewis et al., 2004; Niu, S. et al., 2010; Sim et al., 2024; Koračin et al., 2001; Kunkel, 1984). Data assimilation

techniques have also improved the prediction of stratus sea fog to some extent (Xu et al., 2025). Several studies have employed these models in combination with sensitivity tests to investigate the influence of different meteorological factors on sea fog development. Guo et al. (2021) pointed out that the WRF model can well simulate the cloud water distribution of sea fog, which is basically consistent with the MODIS satellite image. The low-level southerly jet, cold center and strong warm advection are the key factors for the formation of sea fog, while the appearance of westerly wind and the input of dry air lead to the dissipation of sea fog. Kim et al. (2021) used a two-way coupling approach with WRF and ROMS through the Model Coupling Toolkit (MCT). Their results indicated that air-sea coupling significantly improved the accuracy of sea fog simulations, providing more realistic oceanic conditions that better represented the actual fog processes.

Despite the successes of numerical models in simulating temperature and humidity conditions (Gao et al., 2023), the visibility associated with sea fog is not typically included as an output variable. Visibility, however, is a key indicator of sea fog's impact. Recent research has focused on improving diagnostic methods to quantify visibility based on critical fog parameters such as aerosol concentration, liquid water content, and the optical properties of the fog. Gultepe et al. (2006) addressed this issue by developing a new visibility parameterization scheme for warm fog in NWP models. By incorporating both liquid water content (LWC) and droplet number concentration (Nd), they demonstrated significant improvements in visibility predictions through high-resolution 3D fog model simulations. More recently, Hwang et al. (2023) proposed the Reduced Dark Channel Prior (RDCP) algorithm to estimate sea fog intensity and visibility in real time using images captured by cameras. This method offers a low-cost and reliable alternative to traditional visibility meters, thereby providing an innovative approach to improving sea fog forecasting.

Although sea fog is a common phenomenon along China's coastal regions, comprehensive comparative studies examining differences in similar types of sea fog across various sea areas remain limited. Such comparative analyses are essential for improving the accuracy of regional sea fog forecasts. To address this gap, this study investigates two representative advection sea fog events: one occurring along the Zhejiang coast in March 2018 and another in the Qiongzhou Strait in January 2021. Using the WRF model, the research simulates the meteorological conditions associated with fog formation and explores approaches to its numerical prediction. By comparing the weather evolution and formation mechanisms of these two events, the study aims to enhance understanding of sea fog dynamics and provide a scientific basis for improving objective forecasting of low-visibility coastal weather.

The structure of this study is organized as follows: Section 2 outlines the data sources and selected case studies, with

observational and reanalysis datasets being systematically introduced. Section 3 details the visibility diagnostic algorithms and the numerical simulation configurations implemented in the WRF model, including parameterization schemes and domain settings. In Section 4, comparative analyses are conducted to examine the distinct synoptic patterns, thermodynamic characteristics, and atmospheric stability indices associated with fog formation mechanisms. The results of the parts following Section 4.2 are all derived from simulations using the WRF model. Section 5 presents the application of visibility parameterizations to numerical outputs, followed by a quantitative evaluation of algorithm performance through statistical metrics. Finally, key findings and discusses implications for improving fog predictability are synthesized in Section 6, with limitations and future research directions being critically addressed.

2 Data and case overview

2.1 Data sources

In this study, ground-based full-element infill data from hourly station observations of the MICAPS (Meteorological Information Comprehensive Analysis and Process System) are used to obtain visibility information for foggy areas. This dataset, which includes information such as station ID, longitude, latitude, total cloud cover, and visibility, is used for normalized ground mapping. Missing values in the dataset are denoted by the value 9,999. To handle these missing values, quadratic interpolation is applied in this research for data correction.

We utilize the infrared radiance data obtained from the Advanced Geostationary Radiation Imager (AGRI) aboard the FY-4A (Fengyun-4A) satellite, which is China's second-generation geostationary satellite. FY-4A uses a dual-scanning mirror mechanism to achieve precise two-dimensional pointing and is capable of rapid area scanning at minute-level intervals. The FY-4A AGRI L1 full-disk data are first-level (L1) products acquired by FY-4A's multi-channel scanning imaging radiometer, with a 15-min full-disk scanning interval, allowing for high-frequency observations that are especially suited for real-time monitoring of rapidly changing weather systems. This study uses satellite data with a spatial resolution of 4 km, which meets the temporal and spatial resolution requirements for dynamic monitoring of coastal sea fog. In processing the satellite radiation data, we first perform geometric correction for each band using geostationary orbit (GEO) calibration data and remote sensing image processing software. Then, the corresponding pixel values from the 14 channels of FY-4A are extracted based on the latitude and longitude information. Since the nominal data (NOM) grayscale pixel values in FY-4A are indexed according to the calibration table, these indices are used to obtain the brightness temperature or reflectance values from each band's calibration table. Additionally, the FY-4A satellite employs the geostationary nominal projection defined by the CGMSLRIT/HRIT global standard, and its geographic coordinates are calculated based on the WGS84 reference ellipsoid during mapping.

In the analysis of the weather situation, this study utilizes the fifth-generation global climate reanalysis data (ECMWF

Reanalysis v5, or ERA5) provided by the European Centre for Medium-Range Weather Forecasts (ECMWF). This dataset has an hourly temporal resolution and a spatial resolution of 0.25°. With its high temporal and spatial resolution, ERA5 can accurately capture the weather conditions associated with extreme weather events.
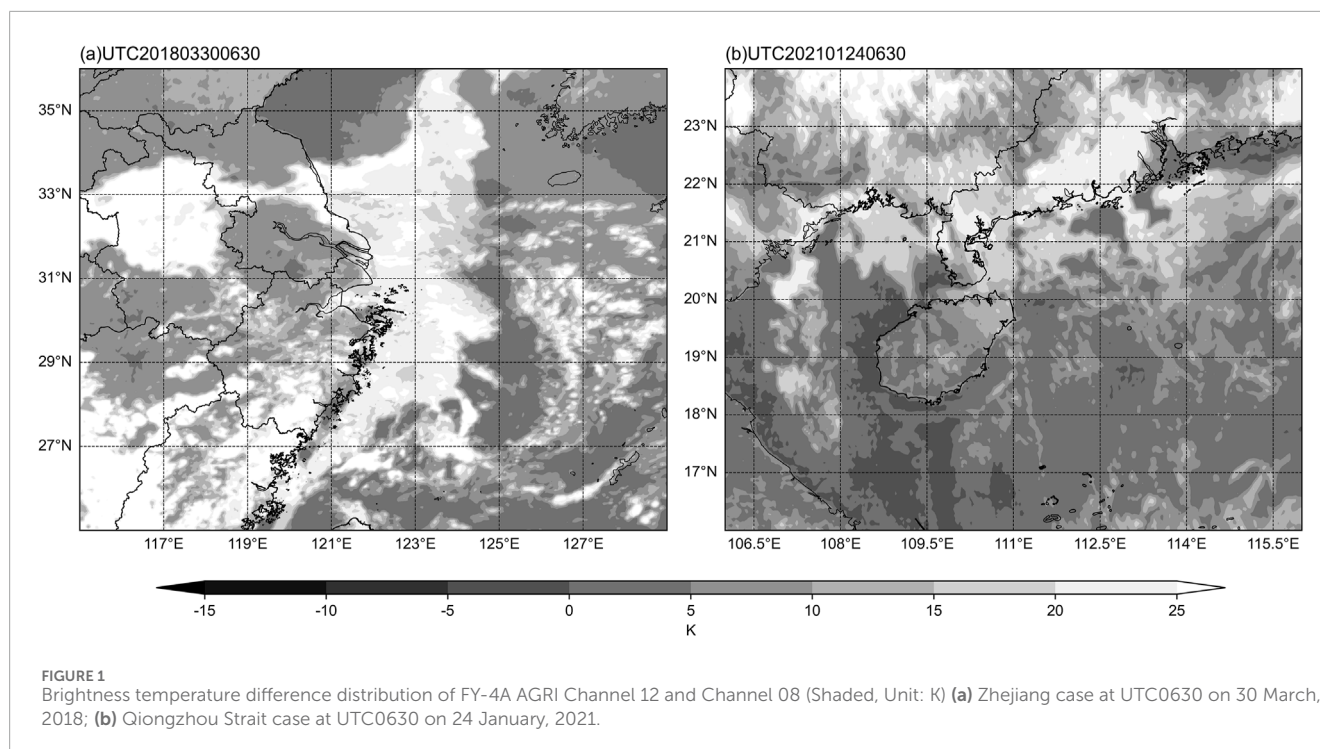
For the numerical simulation, this study uses GFS (Global Forecast System) data with a spatial resolution of 0.25° × 0.25° and a temporal resolution of 6 h to drive the WRF (Weather Research and Forecasting) model. The GFS, developed and operated by the National Centers for Environmental Prediction (NCEP), is a global numerical weather prediction model that provides forecasts ranging from 0 to 240 h. GFS data are widely used in weather analysis, forecasting, and climate research. Its forecast fields not only provide initial and boundary conditions for ocean and wave prediction systems but also offer both deterministic and probabilistic guidance for global weather forecasting. Therefore, GFS data are suitable for providing initial and boundary conditions for the numerical simulation of sea fog events in this study.

In summary, this study utilizes MICAPS station visibility data to analyze the differences in visibility and the evolution of sea fog in two case study areas. Satellite data are employed to monitor the regional shape and characteristics of sea fog and serve as a reference for the numerical simulation of foggy areas. ERA5 data, including the geopotential height and wind fields, are used to analyze the weather conditions during sea fog events. The GFS data are used to drive the mesoscale numerical model WRF for simulation experiments, and the physical quantities derived from the simulation results are applied to analyze the sea fog formation mechanisms and predict visibility.

2.2 Case overview

From March 27 to 2 April, 2018, the coastal region of Zhejiang experienced a typical advection-cooling fog event. Observational data showed that the sea fog exhibited a significant diurnal cycle, with a band-like distribution along the Zhejiang coastline and a clear gradient in intensity, stronger to the north and weaker to the south. As a result, the Yangtze River Estuary shipping channel was forced to close, causing thousands of vessels to be stranded in Shanghai port, leading to significant economic losses in regional shipping. This fog event displayed typical characteristics such as low visibility (with the minimum visibility less than 500 m), extensive coverage, and a prolonged duration.

From January 20 to 26, 2021, a persistent sea fog event occurred in the Qiongzhou Strait, characterized by the combined development of frontal fog and advection fog, resulting in the long-lasting duration of the dense fog. During the frontal fog phase, the center of moisture convergence was located from the southern coast of the Qiongzhou Strait to the northeastern part of Hainan Island, where the dense fog first developed over land. In the advection fog phase, the moisture convergence center shifted to the northern coast of the Qiongzhou Strait and the eastern sea area of Hainan Island, where the fog developed from the sea. This study only simulates the advection fog phase of the sea fog process, and, in conjunction with the Zhejiang sea fog case, explores the development mechanism of advection cooling fog.

FIGURE 1
Brightness temperature difference distribution of FY-4A AGRI Channel 12 and Channel 08 (Shaded, Unit: K) **(a)** Zhejiang case at UTC0630 on 30 March, 2018; **(b)** Qiongzhou Strait case at UTC0630 on 24 January, 2021.

Feature selection analysis shows that the combination of brightness temperature difference (DBT) and texture parameter (STD BT10.80) can effectively improve the model's ability to distinguish sea fog and low clouds (Wang et al., 2023; Ryu and Hong, 2020; Li et al., 2023). Sea fog detection typically uses thermal infrared (3.9 μm) and mid-infrared (11.2 μm) bands. Due to the small size of fog particles (He et al., 2022), the brightness temperature of fog in the 3.9 μm band is significantly lower than that in the 11.2 μm band. In contrast, cloud particles are larger, and their brightness temperatures are nearly identical in these two bands. Therefore, the brightness temperature difference method using the 3.9 μm and 11.2 μm bands, as well as the pseudo-ratio emissivity method using the 3.9 μm band, can effectively identify fog of varying intensities. This approach is especially effective under low visibility conditions, as it improves detection accuracy and reduces false positives. In the FY-4A satellite, Channel 08 corresponds to the mid-wave infrared band around 3.7 μm, and Channel 12 corresponds to the long-wave infrared band around 11.2 μm. By analyzing the brightness temperature difference between Channel 08 and Channel 12, the distribution of fog areas can be clearly identified, with positive values indicating fog zones. This study uses FY-4A satellite brightness temperature difference images to display the coverage of the fog areas, as shown in Figure 1.

FY-4A satellite monitoring results at 0630 UTC on 30 March, 2018 show that the sea fog in Zhejiang is characterized by a wide distribution in the north and narrow distribution in the south. The fog area extends along the coastline and the edge is smooth. The monitoring results at 0630 UTC on 24 January, 2021 show that the Qiongzhou Strait sea fog covers a uniform and smooth cloudy area, and the fog area covers the Qiongzhou Strait, the Yongle Peninsula and its surrounding waters, as well as the northeast of Hainan Island.

3 Methodology and experimental design

3.1 Methodologies

The Weather Research and Forecasting (WRF) model is a widely used mesoscale numerical weather prediction system, applied extensively in regional and local weather forecasting as well as atmospheric research. It offers high spatial resolution, a flexible modular structure, and advanced data assimilation capabilities. WRF supports multiple nested grids, allowing for the precise simulation of multiscale atmospheric processes. It is commonly employed in simulations of extreme weather events, environmental forecasting, and climate studies. In this study, the ARW (Advanced Research WRF) version 4.1, which is well-suited for both research and practical forecasting applications, is utilized.

The visibility algorithms used in this study are as follows (Bang et al., 2008):

(1) SW99 Algorithm: The SW99 visibility algorithm, proposed by Steolinga and Warner in 1999, calculates visibility based on liquid water content. This algorithm considers the impact of various hygroscopic substances on the extinction coefficient. This algorithm incorporates the effects of various hygroscopic substances on the extinction coefficient. To compute this, different exponents are applied to each water vapor species, with the specific exponents derived from their corresponding extinction coefficients. The equation governing this calculation is given below:

$$\text{vis} = \frac{-\ln(0.02) * 1000}{144.7q_{\text{cloud}}^{0.88} + 1.1q_{\text{rain}}^{0.75} + 163.9q_{\text{ice}}^{1.0} + 10.4q_{\text{snow}}^{0.78}} \quad (1)$$

In the equation, q_{cloud} represents the cloud water mixing ratio, which is defined as the mass of cloud water per unit mass of air. Similarly, q_{rain} refers to the rainwater mixing ratio, indicating the mass of rainwater per unit mass of air. The ice crystal mixing ratio, denoted by q_{ice}, describes the mass of ice crystals per unit mass of air, while q_{snow} is the snow mixing ratio, representing the mass of snow per unit mass of air. All of these variables are expressed in kg/kg. Finally, the visibility, derived from this formula, is given in meters.

(2) FSL Algorithm: The FSL (Forecast Systems Laboratory) visibility algorithm calculates visibility by considering factors such as temperature, dew point temperature, and relative humidity (Pahlavan et al., 2021). It applies a decremental averaging method to correct the temperature and dew point values used in the formula, and recalculates the relative humidity, thereby improving forecast accuracy. In this study, variables from numerical simulation results are substituted into both algorithms for calculation to compare the application effectiveness of the two algorithms in the two sea fog cases. The FSL algorithm is based on the relative humidity (RH) and the temperature-dew point difference, as shown by the following equation:

$$\mathbf{vis} = 1.609344 * 6000 * \frac{\mathbf{T} - \mathbf{T_d}}{\mathbf{RH^{1.75}}} * 1000 \qquad (2)$$

where T represents the temperature, T_d represents the dew point temperature, the unit is K; RH represents relative humidity in %.

3.2 Experimental settings

The WRF model has been widely applied in numerical simulations of sea fog along China's coastline. In this study, the WRF model is configured with a spatial grid resolution of 3 km, with a grid size of 551 × 461 points, and a time step of 15 s. The model's top layer is set at 1,000 Pa, with a total of 50 vertical layers. The simulation period for the Zhejiang case spans from 0600 UTC to 1800 UTC on March 29 to 30, 2018, with a total integration time of 36 h; the simulation period for the Qiongzhou Strait case is from 0600 UTC to 1800 UTC on January 23 to 24, 2021, also with a 36-h integration time. The Zhejiang case, located in the mid-latitude region, uses the Lambert conformal conic projection, while the Qiongzhou Strait case, located in the low-latitude region, uses the Mercator cylindrical projection. The regional settings and terrain heights are shown in Figure 2, and the physical parameterization schemes used in the model are listed in Table 1.

4 Comparative analysis of sea fog cases

4.1 Fog conditions

According to the classification standards for fog forecasts set by the CMA (China Meteorological Administration), the levels are defined as follows: light fog (1,000 m ≤ visibility < 10,000 m), moderate fog (500 m ≤ visibility < 1,000 m), dense fog (200 m ≤ visibility < 500 m), strong dense fog (50 m ≤ visibility < 200 m), and extremely dense fog (visibility < 50 m).

For the Zhejiang sea fog case, the Yuhuan and Dachen meteorological stations were selected as representative stations to analyze the actual visibility conditions of coastal sea fog. Analysis of the hourly visibility data from the MICAPS system, from UTC1800 on March 26 to 0600 UTC on 2 April, 2018, reveals that (Figure 3) dense fog with visibility less than 1 km first occurred at the Dachen station at UTC1800 on March 27. Subsequently, both Dachen and Yuhuan stations experienced light fog, and from UTC1600 on March 29, Dachen station monitored dense fog for a duration of 20 h. Between UTC1100 on March 31 and 0000 UTC on April 1, visibility at both Yuhuan and Dachen stations remained at low levels. The evolution of visibility throughout the entire development of this dense fog event demonstrates that, under stable weather conditions, the daily duration of sea fog exhibited significant fluctuations.

For the Qiongzhou Strait sea fog case, the Xuwen and Haikou meteorological stations were selected as representative stations to analyze the actual visibility conditions of the Qiongzhou Strait sea fog. Analysis of the hourly visibility data from the MICAPS system, from 1800 UTC on January 19 to 0600 UTC on 26 January, 2021, reveals that (Figure 3), from 0600 UTC on January 20, the visibility at both stations began to decrease to below 5 km. After 1000 UTC on January 20, the visibility at both stations showed a highly similar development trend for the next 42 h. Haikou station first observed dense fog at 1300 UTC on January 21, and thereafter, both stations continued to monitor persistent dense fog, with brief periods of strong dense fog. Overall, the visibility at Xuwen station was lower than that at Haikou station, remaining consistently below 5 km after 1000 UTC on January 20, with no apparent diurnal variation.

During the Zhejiang sea fog event, a stable weak high-pressure system was positioned between the northern Zhejiang coast and Japan, with its center intensity around 1,028 hPa, dominating the sea fog formation (Figure 4). The easterly flow around this high-pressure system transported warm and moist air (Figure 6a) from the sea surface to the Zhejiang coastline. At the 500 hPa level, the meteorological conditions were stable, with the subtropical high's 588-line retreating southward over the sea, and no prominent circulation centers in the northern region. The East Asian trough had shifted to the Bering Sea in the western Pacific, leaving a shallow trough active in the region. At higher altitudes, there was no significant trough-ridge activity. The continuous influx of weak cold air at the surface helped maintain the weak high-pressure system, while the tropical cyclone "Jelawha" in the northwest Pacific obstructed the system's eastward movement. This stable weather pattern created favorable conditions for the persistence of sea fog.

During the sea fog event in the Qiongzhou Strait, a high-pressure system was positioned over the northeastern Korean Peninsula at the surface, with the Qiongzhou Strait situated to the south of this system, under the influence of both northeast and southeast airflows (Figure 5). As depicted in Figure 6b, these airflows facilitated the advection of warm, moist air into the Qiongzhou Strait. The entire region, including both the Qiongzhou Strait and Hainan Island, was within a nearly uniform pressure field, with a slight pressure gradient stabilizing at 1,016 hPa. At the 500 hPa level, the East Asian trough had shifted eastward toward the Japan Sea, while the Qiongzhou Strait experienced the influence of northwest airflow behind the trough.
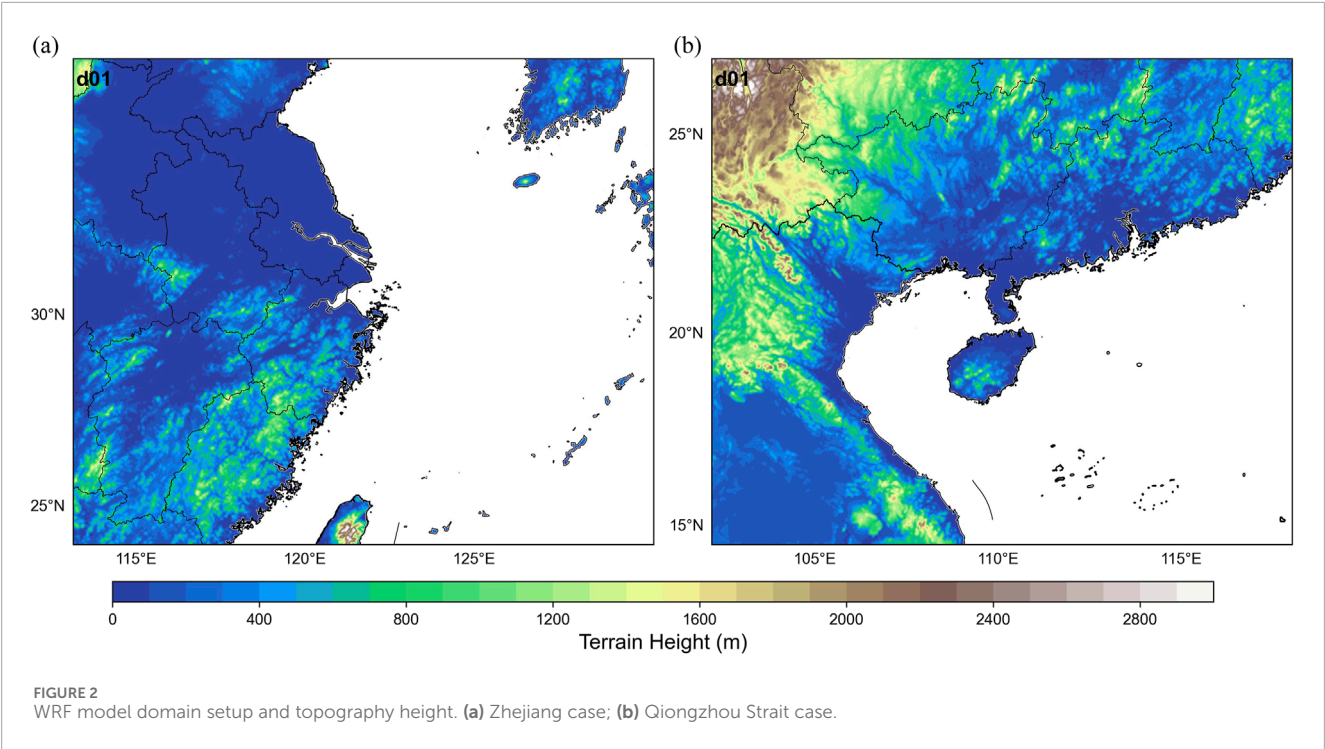
FIGURE 2
WRF model domain setup and topography height. **(a)** Zhejiang case; **(b)** Qiongzhou Strait case.

TABLE 1 Model physical parameterization scheme selection.

Model scheme	Scheme option
Micro physics scheme	Lin (Chen and Sun, 2002)
Planetary boundary layer scheme	YSU (Hong et al., 2006)
Cumulus parameterization scheme	Kain–Fritsch (Kain, 2004)
Shortwave scheme	Dudhia (Dudhia, 1989)
Longwave scheme	RRTM (Mlawer et al., 1997)
Land Surface scheme	Noah–MP (Yang et al., 2011)
Surface layer scheme	Revised MM5 (Jiménez et al., 2012)

4.2 Thermal conditions

Air–sea temperature difference played an important role in regulating the formation and dissipation of sea fog (Han and Zhang, 2022). Previous studies have demonstrated that both warm air moving over cold seas and cold air moving over warm seas can contribute to the formation of sea fog. Fog that forms when the surface air temperature (SAT) exceeds the sea surface temperature (SST) is referred to as warm advection fog. This type of fog occurs when heat is transferred from the warm, saturated air above to the sea surface through turbulent diffusion (mechanical turbulence), resulting in the cooling of the air near the surface. Once warm advection fog has largely formed, the warm, moist air is maintained through strong advection over the cold sea surface. In contrast,

when the surface air temperature (SAT) is lower than the sea surface temperature (SST), the fog is classified as cold advection fog.

From Figures 6c,d, it can be observed that in both cases, the surface air temperature (SAT) in the fog-affected region exceeds the sea surface temperature (SST). This indicates that the sea fog events along the Zhejiang coast and in the Qiongzhou Strait are both instances of warm advection fog, also referred to as advection cooling-type sea fog. In this type of fog, warm air moves over cold sea surfaces, causing the water vapor within the air mass to condense, thereby forming fog. As a result, the fog is typically dense, with a large coverage area, long duration, and low visibility. The shape of the negative temperature difference region in the figures closely corresponds to the fog region observed by satellite, further supporting the conclusion that the advection cooling effect is the primary cause of the formation of these two sea fog events.

Figures 6a,b present the distribution of sea surface temperature (SST) at 0000 UTC on 30 March, 2018. It is evident that along the Zhejiang coast, the SST gradient is pronounced, with temperatures decreasing from 300 K to approximately 280 K, indicating a clear downward trend. This cold sea surface provides a large-scale cooling condition conducive to the formation of advection cooling fog. In contrast, the SST gradient in the Qiongzhou Strait case is less pronounced.

4.3 Water vapor and fog vertical structure

The direction of the water vapor flux vectors indicates that the water vapor in both fog cases originates from the evaporation of the ocean surface (Figures 7a,b). Along the Zhejiang coast, the water vapor is primarily transported from the northeast (Figure 7a). This is due to the development of a tropical storm in the western
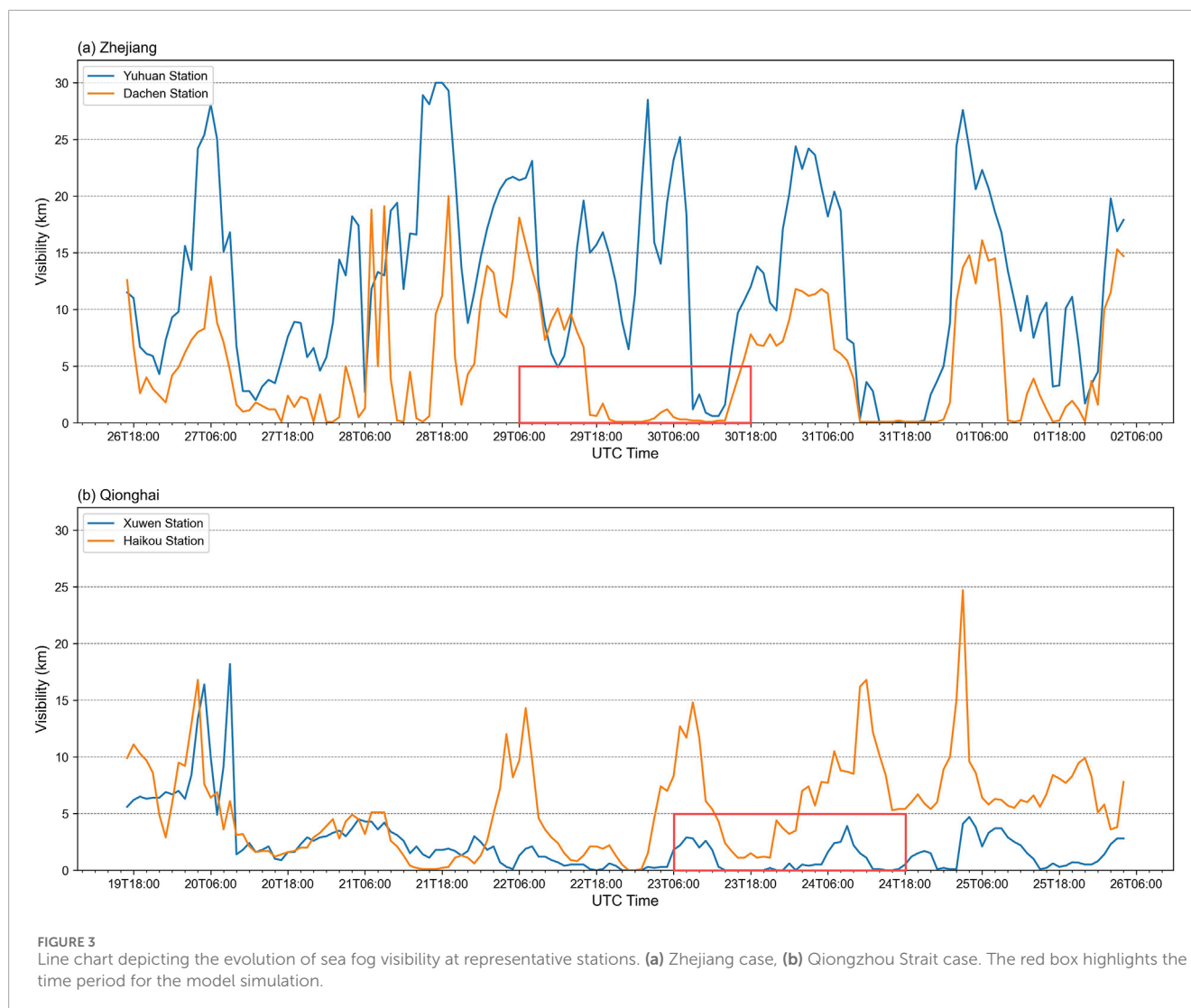
FIGURE 3
Line chart depicting the evolution of sea fog visibility at representative stations. **(a)** Zhejiang case, **(b)** Qiongzhou Strait case. The red box highlights the time period for the model simulation.
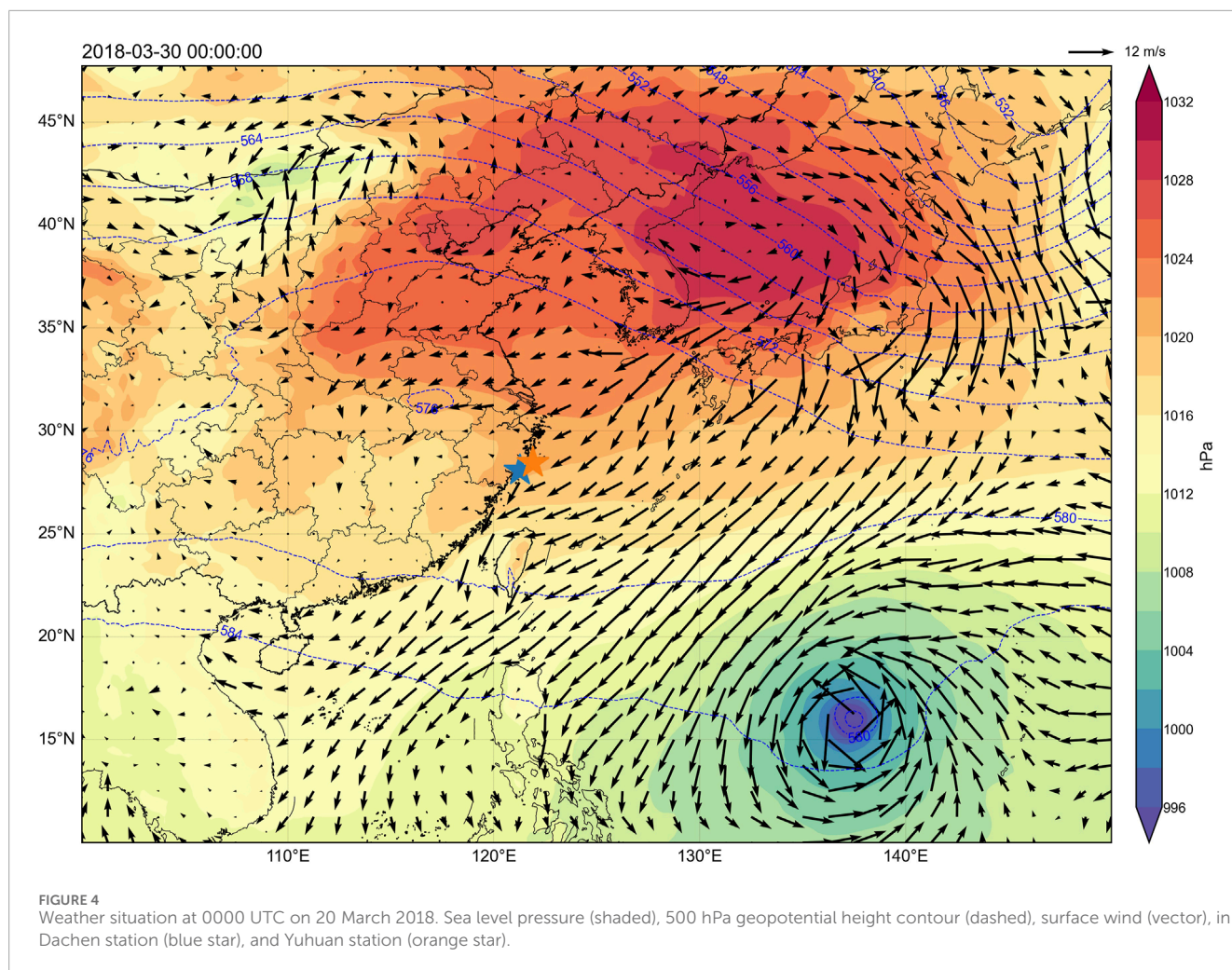
Pacific Ocean east of the Philippines (Figure 4), where the easterly winds on the outskirts of the low-pressure system continuously transport warm and moist air to the Zhejiang coast. At the same time, the region with 100% relative humidity at 2 m above the ground shows a distinct north-wide, south-narrow banded distribution.

On the western side of the Qiongzhou Strait, there is a strong warm advection (Figure 7b). Above the warm current, the water vapor flux values are high, making it easy for water vapor to condense into fog. Influenced by the easterly wind, the water vapor converges primarily on the northwest side of the Qiongzhou Strait. The region of high relative humidity is distributed along the coastline, and the wind blowing from the ocean to the land transports ample water vapor to the Leizhou Peninsula, explaining the formation of dense fog later on the land north of the Leizhou Peninsula. A comparison of the low-level relative humidity distribution in the two cases shows that the humidity conditions along the Qiongzhou Strait coast are better than those along the Zhejiang coast, with a larger difference in relative humidity between the sea and land (Figures 7c,d).

Sufficient water vapor content is the basis for cloud water formation. The standard for diagnosing fog areas is generally a cloud water mixing ratio of no less than 0.016 g/kg. In this study, the model's lowest layer (QCLOUD) variable was analyzed, and the threshold for cloud water mixing ratio was set to 0.016 g/kg to examine the horizontal and vertical structures of fog cases.

The diurnal variation of the Zhejiang fog coverage area is small (Cao et al., 2022). The simulation results closely matched the fog area observed in the satellite cloud images and reasonably reflected the occurrence range and timing of the fog. A section was taken from the fog occurrence region (120.0°E, 30.0°N) to (126.0°E, 34.0°N), where the fog top height is mostly around 400 m (Figures 8a,b). Near (125°E, 34°N), the cloud water mixing ratio is low, but the height extends to greater altitudes, with the maximum fog top reaching more than 900 m.

Compared to the Zhejiang fog case, the Qiongzhou Strait fog occurrence area is closer to the land, with a maximum cloud water mixing ratio of about 0.4 g/kg. For the Qiongzhou Strait case, a profile was taken from the fog occurrence region (109.4°E, 22.0°N) to (110.61°E, 19.02°N), extending from the model's lowest layer to

FIGURE 4
Weather situation at 0000 UTC on 20 March 2018. Sea level pressure (shaded), 500 hPa geopotential height contour (dashed), surface wind (vector), in Dachen station (blue star), and Yuhuan station (orange star).

higher altitudes (Figures 8c,d). The fog top height reaches up to 400 m. It is evident that the near-surface cloud water mixing ratio region in the Qiongzhou Strait case extends to a greater height than in the Zhejiang case, and the thickness of the fog is also larger.

4.4 Atmospheric stratification conditions

Warm air moves horizontally over cold surfaces or air layers, causing the lower layer of the warm air to cool rapidly when it comes into contact with the cold sea surface. This cooling effect is more pronounced at the bottom layer, while the upper layers cool more slowly. As a result, an inversion layer is formed. In the Zhejiang case, the temperature-dewpoint temperature profile was plotted for the point at (123°E, 32°N), as shown in Figure 8a. During the fog event, a significant inversion layer persisted at this location, with its height predominantly below 800 hPa. According to the simulation results from 0000 UTC on 30 March, 2018, within the 50 vertical levels simulated by the model, the temperature-dewpoint difference for the first eight layers (i.e., below 915 hPa) was less than 5°C, with the minimum value being 0.71°C. This small temperature-dewpoint difference indicates favorable humidity conditions for fog formation in this layer. The inversion layer gradually developed
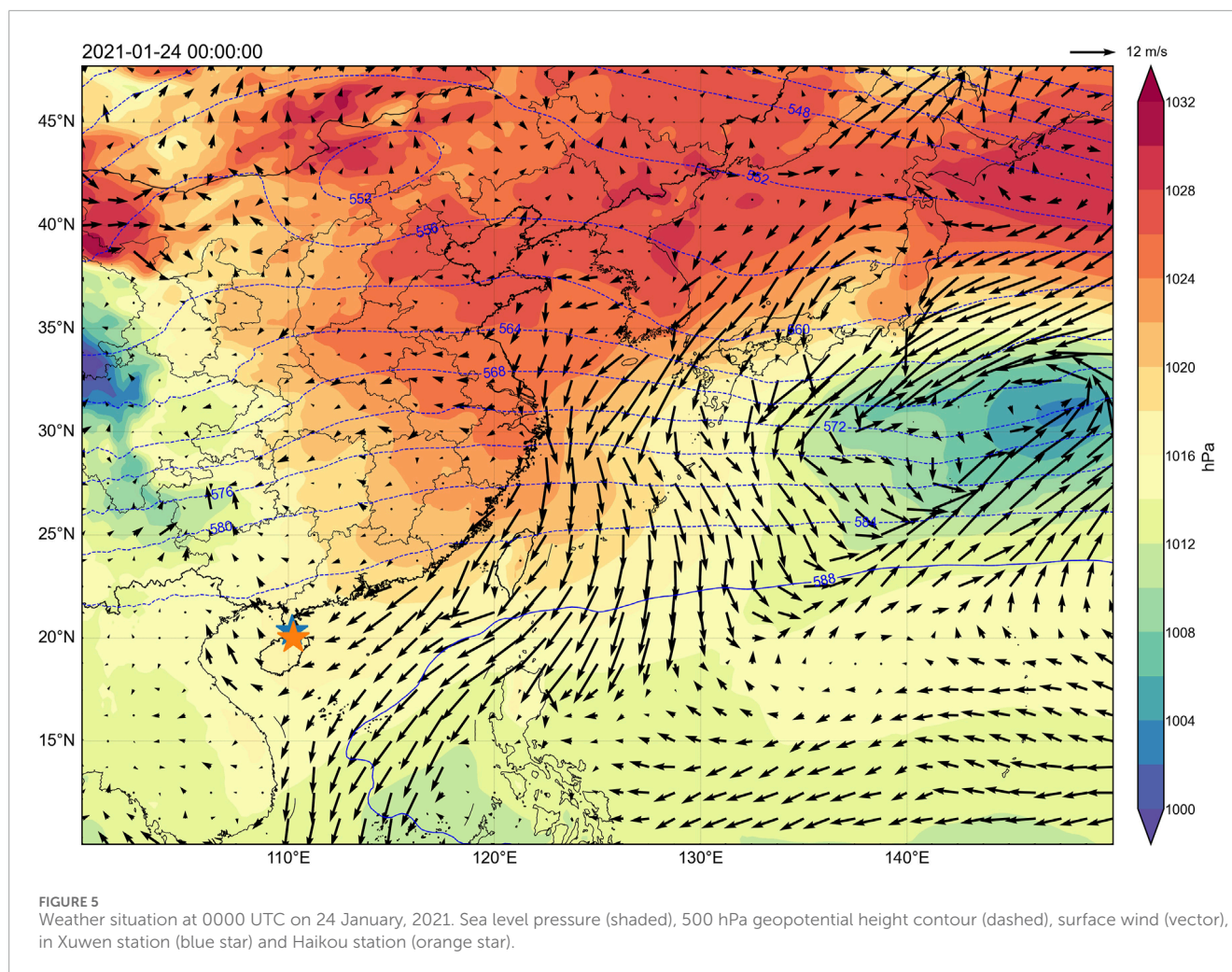
on March 30 (Figure 9). At 0000 UTC, the temperature between 900 hPa and 800 hPa showed little variation with height; by 1200 UTC, the inversion layer had fully formed and became more pronounced.

In the two cases, relevant physical quantities from the WRF model outputs were extracted to calculate the equivalent potential temperature. The equivalent potential temperature serves as a stability indicator. In the stable atmosphere, the equivalent potential temperature either remains relatively constant or increases with height, as observed in temperature inversion layers, whereas in an unstable atmosphere, it generally decreases with height.

In the Zhejiang Strait case, a vertical section was taken from (120.0°E, 30.0°N) to (126.0°E, 34.0°N) (as shown in Figure 8a), and the vertical section of the equivalent potential temperature was obtained (Figure 10). Near (124.0°E, 32.68°N), the equivalent potential temperature in a certain region increases significantly with height (i.e., the vertical gradient $\frac{\partial \theta_e}{\partial z} > 0$), covering the height range from below 900 hPa to above 850 hPa. From 0000 UTC to 1200 UTC, the trend of equivalent potential temperature increasing with height strengthened, and the starting position of the stable stratification lowered, with its thickness increasing accordingly.

In the Qiongzhou Strait case, a vertical section was taken from (109.4°E, 22.0°N) to (110.61°E, 19.02°N) (as shown in Figure 8c),

FIGURE 5
Weather situation at 0000 UTC on 24 January, 2021. Sea level pressure (shaded), 500 hPa geopotential height contour (dashed), surface wind (vector), in Xuwen station (blue star) and Haikou station (orange star).

and the vertical section of the equivalent potential temperature was obtained (Figure 10). At 0000 UTC on the 24th, from about 810 hPa to 780 hPa, the equivalent potential temperature increases with height. By 0600 UTC on the 24th, the lower layers of the atmosphere showed an increase in equivalent potential temperature, with some regions above 820 hPa showing an increase with height, indicating a stable atmospheric state that suppresses vertical mixing, facilitating moisture accumulation near the sea surface and supporting fog persistence. By 1200 UTC on the 24th (Figure 10f), from the surface to 900 hPa, the equivalent potential temperature changes were small, with a vertical difference ≤5 K/100 hPa. Between 850 hPa and 700 hPa, the equivalent potential temperature increased with height, forming a relatively stable inversion layer, with warmer, moist air above and cooler, drier air below. This condition favors the persistence of advective sea fog. Near (110.5°E, 19.26°N), around 900 hPa, there is a region where the equivalent potential temperature increases significantly with height. The stable atmospheric stratification provides favorable conditions for the persistence of the dense fog.

Due to the influence of water vapor, the region where the equivalent potential temperature increases with height does not completely correspond with the latitudinal and longitudinal distribution of the inversion. However, this phenomenon still reflects that in the Zhejiang case, the position of the stable stratification is lower, and the inversion layer is more significant. The Qiongzhou Strait sea fog exhibits enhanced atmospheric stability, characterized by sustained warm advection extending to 950 hPa and intermittent inversion layers aloft, which collectively contribute to marked thermodynamic stratification.

4.5 Turbulence effect

The Richardson number (Ri) is a dimensionless parameter that characterizes the stability of atmospheric flow. It is used to measure the relative importance of dynamic shear effects and thermal stratification effects in a fluid. It is defined as the ratio of thermal stability effects (buoyancy) to dynamic disturbance effects (wind shear), and its mathematical expression is:

$$Ri = \frac{\frac{g}{\theta}\frac{\partial \theta}{\partial z}}{\left(\frac{\partial u}{\partial z}\right)^2 + \left(\frac{\partial v}{\partial z}\right)^2} \tag{3}$$

when Ri > 0.25, the thermal stability stratification dominates, and turbulence is suppressed. When Ri > 1, the mechanical generation term cannot overcome the buoyancy term's limitation to generate
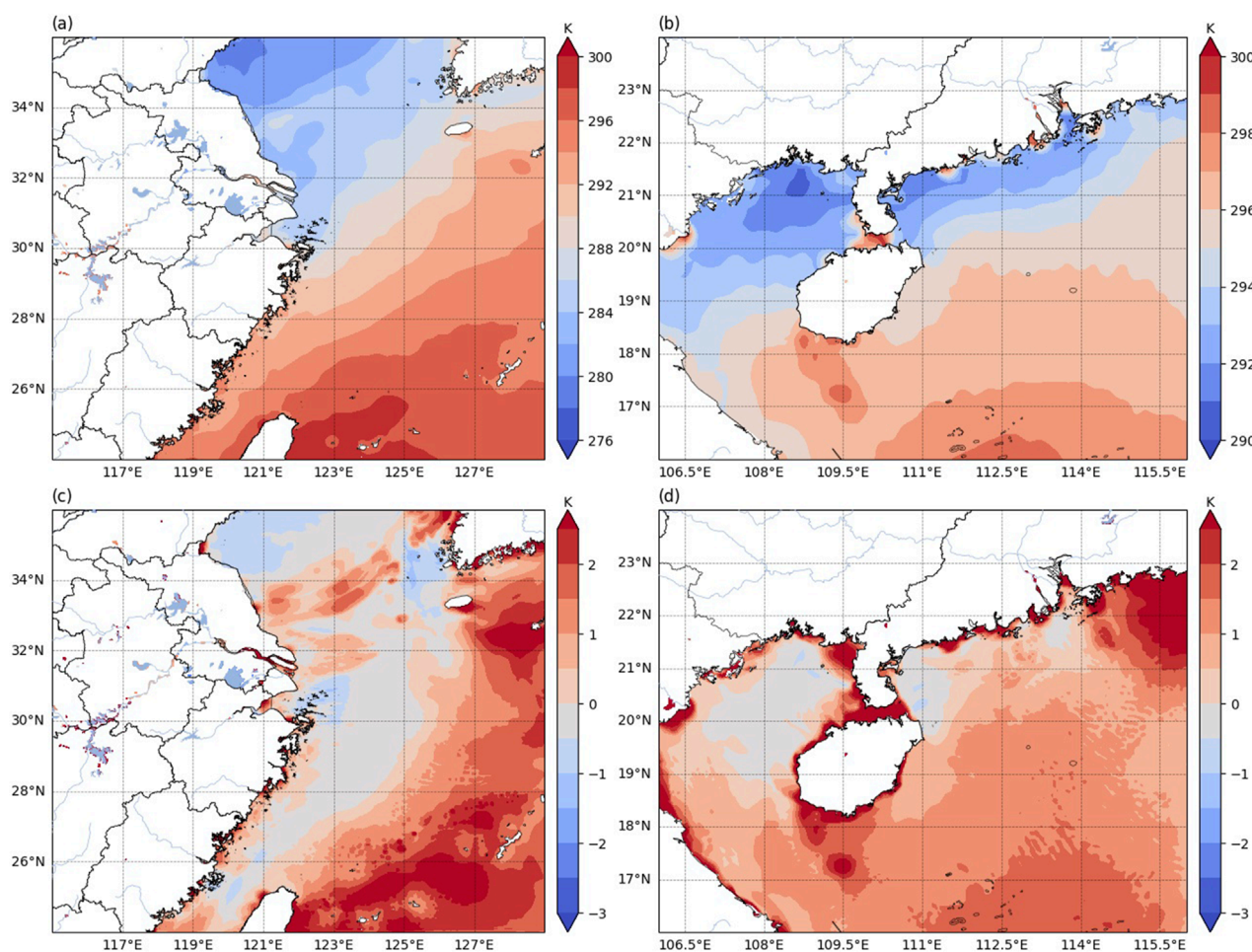
FIGURE 6
Sea surface temperature (color map, unit: K) and air-sea temperature difference (SST minus SAT) (color map, unit: K) distribution for **(a)** Zhejiang case (0000 UTC on 30 March, 2018), **(b)** Qiongzhou Strait case (0000 UTC on 24 January, 2021), **(c)** Zhejiang case air-sea temperature difference, and **(d)** Qiongzhou Strait case air-sea temperature difference.

turbulence. Conversely, when Ri < 0.25, the mechanical generation term can overcome the buoyancy term's limitation, easily triggering turbulence or mixing processes. Small-scale turbulence has an essential role in sea-fog formation and evolution (Huang et al., 2015; Yang and Gao, 2019). The formation of advection-cooled sea fog requires stable thermal stratification, which means that an inversion layer should form at the lower levels to suppress vertical mixing. It also requires moderate wind speeds and small wind shear to reduce turbulence, while still maintaining the advection transport of water vapor. Therefore, the Richardson number can effectively reflect the interaction between thermal stability and dynamic disturbances (Equation 3). In this study, the Richardson number is calculated at the lowest layer of the model (Figure 11), and vertical sections of Ri are extracted at 0000 UTC for two example simulation periods (with section line locations corresponding to Figure 8) for analysis.

There is a region with Ri > 0.25 on the ocean surface along the coast of Zhejiang, and the region with large cloud-water mixing ratio (Figure.8a) is more consistent with the region with Ri > 0.25, showing a zonal distribution of north wide and south narrow. At 0000 UTC and 0600 UTC on March 30 (by which time coastal

advection fog had already formed), under the control of a stable high-pressure system, the high Ri region persisted. This suggests that there was strong turbulence suppression in the fog area, reducing the vertical transport of water vapor and heat, allowing humidity to continuously accumulate near the sea surface. The stable weather conditions under high pressure favor the long-term persistence of sea fog.

In the lower atmosphere near (125°E, 33.34°N), there is a relatively low Ri value region (Figure 11c). Compared to the upper atmosphere, there is some turbulent mixing, which facilitates the vertical transport of water vapor and the increase in cloud water mixing ratio (Figure 8b). As the sea fog develops, regions with a high cloud water mixing ratio further enhance atmospheric stability, thereby inhibiting the development of turbulence. This stability feedback mechanism allows the sea fog to persist near the sea surface for extended periods and to gradually expand upward at a slow pace.

On both sides of the Qiongzhou Strait, the coastal areas always maintain Ri > 0.25, and in some places, Ri > 1.0, severely suppressing turbulence. This indicates that when warm air advection reaches the cold sea surface, despite the existence of a sea-air temperature
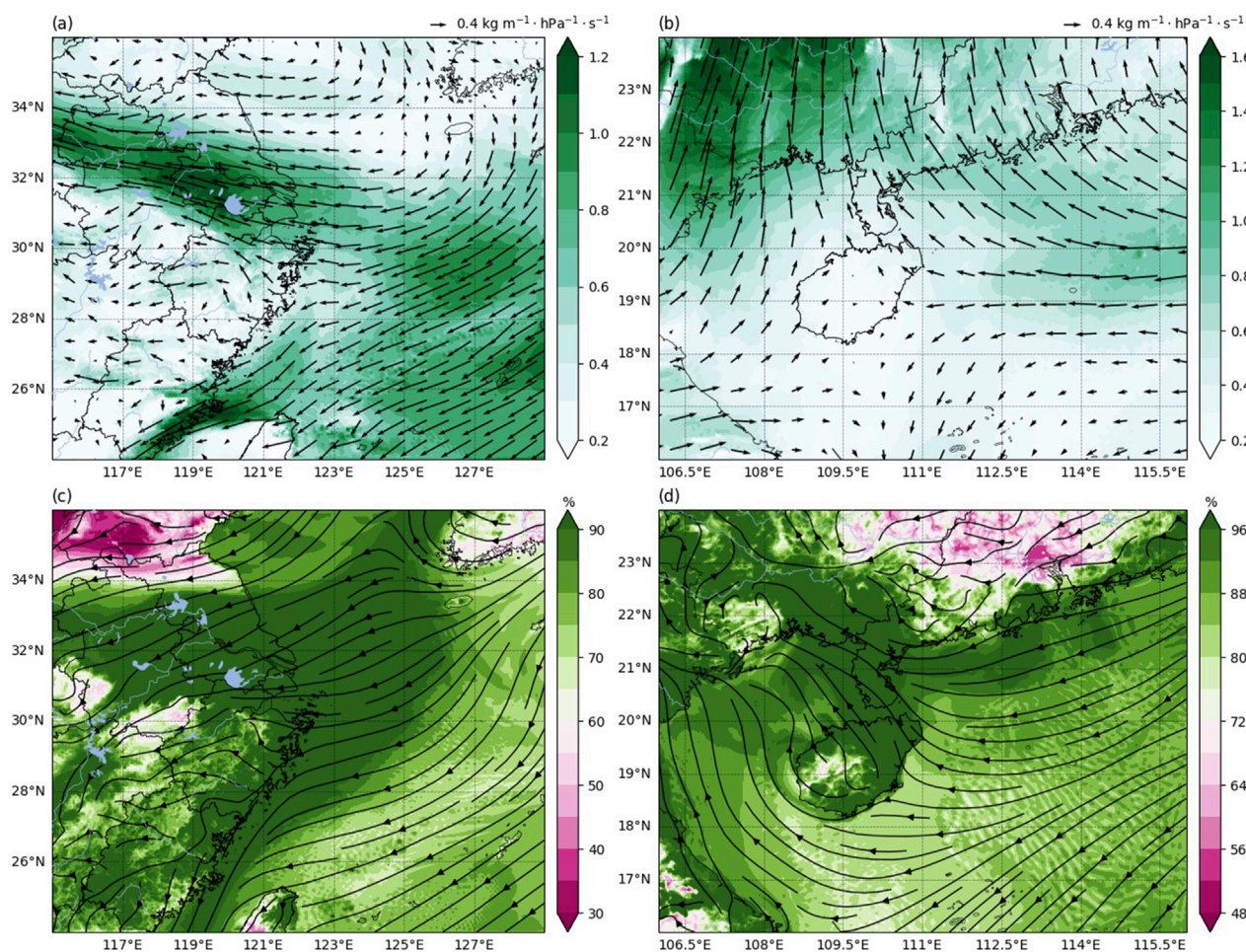
FIGURE 7
Water vapor flux and relative humidity distribution for **(a,c)** Zhejiang case (0000 UTC on 30 March 2018), **(b,d)** Qiongzhou Strait case (0000 UTC on 24 January 2021). Arrows: 850 hPa water vapor flux vectors; shaded in row 1: magnitude of water vapor flux (units: kg/(m·hPa·s)); streamlines: 10 m wind field (units: m/s); shaded in row 2: 2 m relative humidity field (units: %).

difference (SAT > SST), turbulence remains weak (Ri > 0.25), and the cooling effect of the cold sea surface only acts on a very thin layer of air near the surface. This is insufficient to generate a sufficiently thick cooling air layer through vertical mixing, making it difficult to trigger water vapor condensation and form thick advection fog.

From the vertical section (Figure 10f), it can be observed that turbulence begins to form near the surface in the fog area. However, the Ri values at the surface along the section are between 0.25 and 1.0, which is not conducive to further intensifying turbulence. It is also difficult to find a clear relationship between the distribution of Ri and the formation and maintenance mechanism of sea fog in the fog area, suggesting that turbulence is not the main mechanism for the formation of sea fog in this case.

In both inland and oceanic regions, the Ri values in certain areas gradually decrease from morning to noon, transitioning from positive to negative. For example, at 0600 UTC on 24 January, 2021, when solar radiation increased and warm advection entered the Leizhou Peninsula, the inversion layer was weakened or even disappeared (Figure 10b), leading to a decrease in the vertical temperature gradient and a negative heat term, resulting in Ri < 0.

Thus, the formation of advection fog requires moderate turbulence, but significant turbulence suppression is more favorable for maintaining the fog. During the development of sea fog, the stable stratification in high Ri regions helps maintain the height of the fog top, preventing the fog layer from expanding too quickly upward.

5 Comparison of visibility diagnose methods

By comparing the results from the formulas (Figure 12), it can be observed that the shape of the low visibility regions in both examples closely matches the fog area observed in the satellite cloud images, indicating that both SW99 and FSL have some forecasting capability. The key difference lies in the fact that SW99 calculates visibility more precisely, with calculated visibility values distributed across various numerical ranges. However, since SW99 is based on liquid water content as a variable, its predicted fog area shape closely matches the cloud water mixing ratio region at the 0.016 g/kg
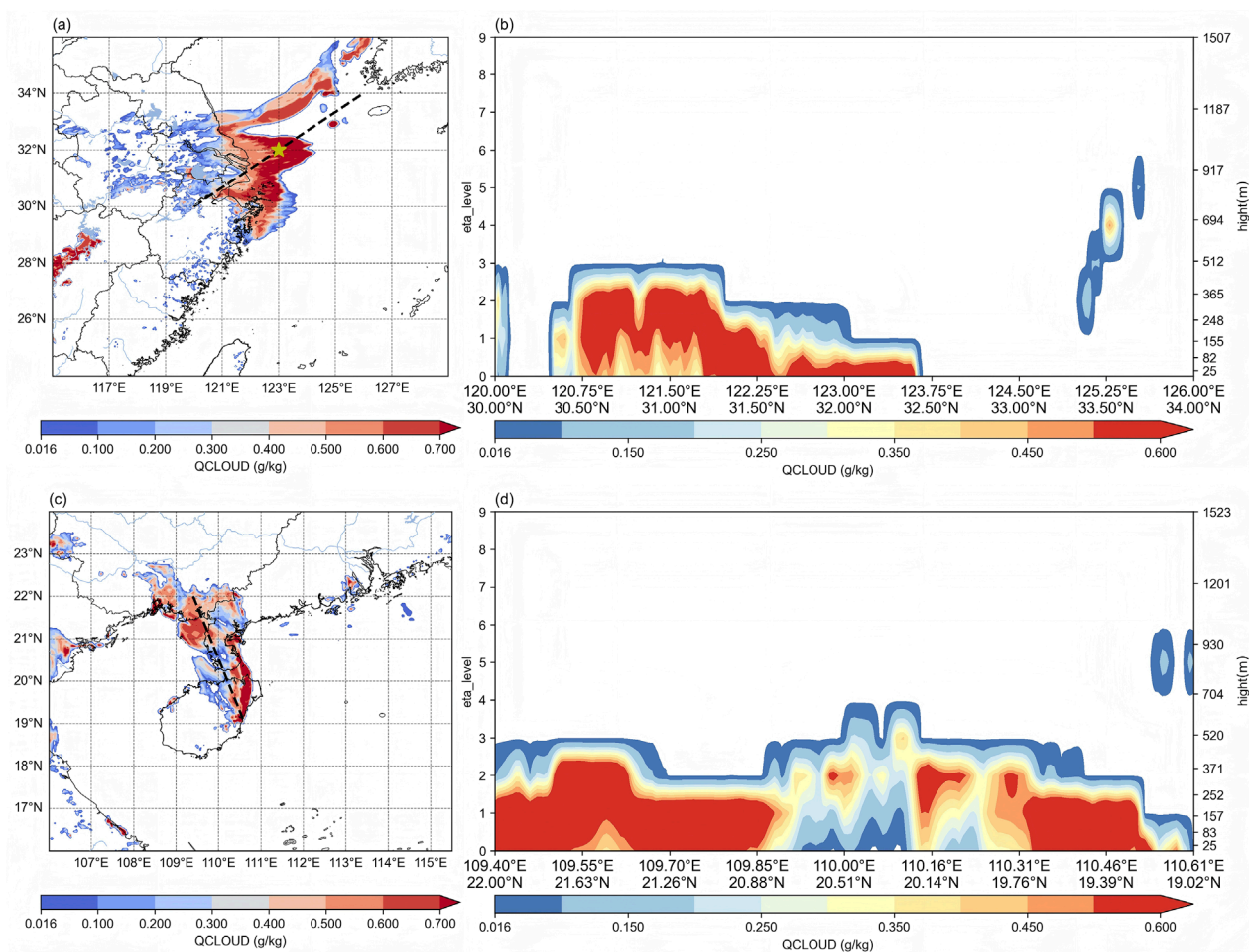
FIGURE 8
Distribution of cloud-water mixing ratios and vertical sections for **(a,b)** Zhejiang case at 0000 UTC on 30 March, 2018; **(c,d)** Qiongzhou Strait case at 0000 UTC on 24 January, 2021.
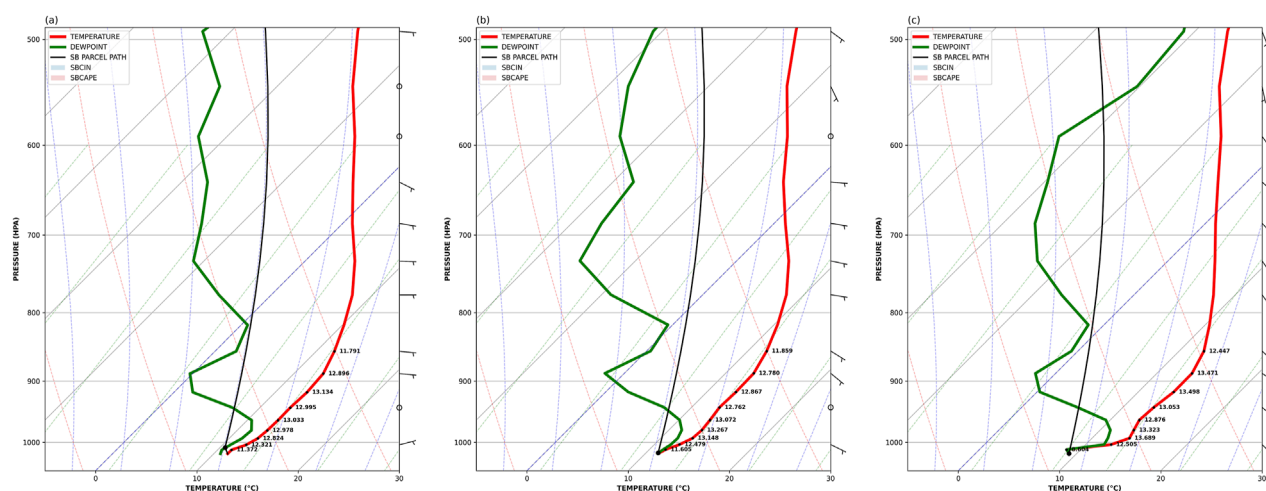

FIGURE 9
Vertical profiles of temperature and dew point temperature for the Zhejiang sea fog case (Temperature unit: °C) at **(a)** 0000 UTC, **(b)** 0600 UTC, and **(c)** 1200 UTC on 30 March, 2018.
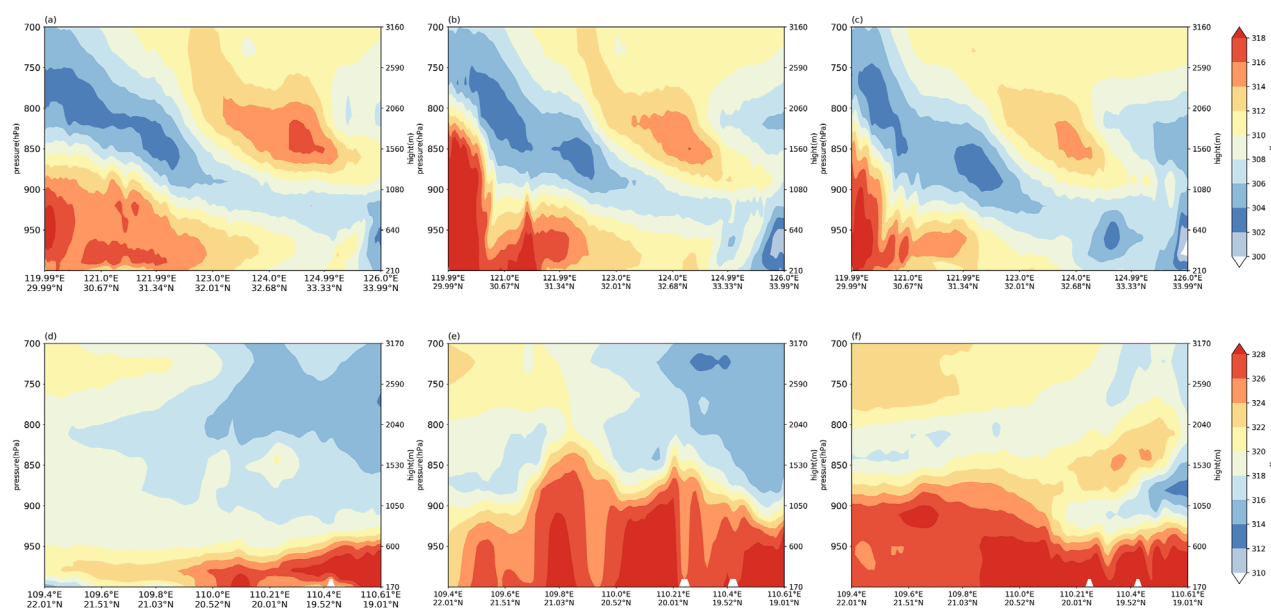
FIGURE 10
Vertical section of the equivalent potential temperature for the Zhejiang sea fog at **(a)** 0000 UTC, **(b)** 0600 UTC, and **(c)** 1200 UTC on 30 March, 2018 and the Qiongzhou Strait sea fog at **(d)** 0000 UTC, **(e)** 0600 UTC, and **(f)** 1200 UTC on 24 January, 2021 (unit: K).
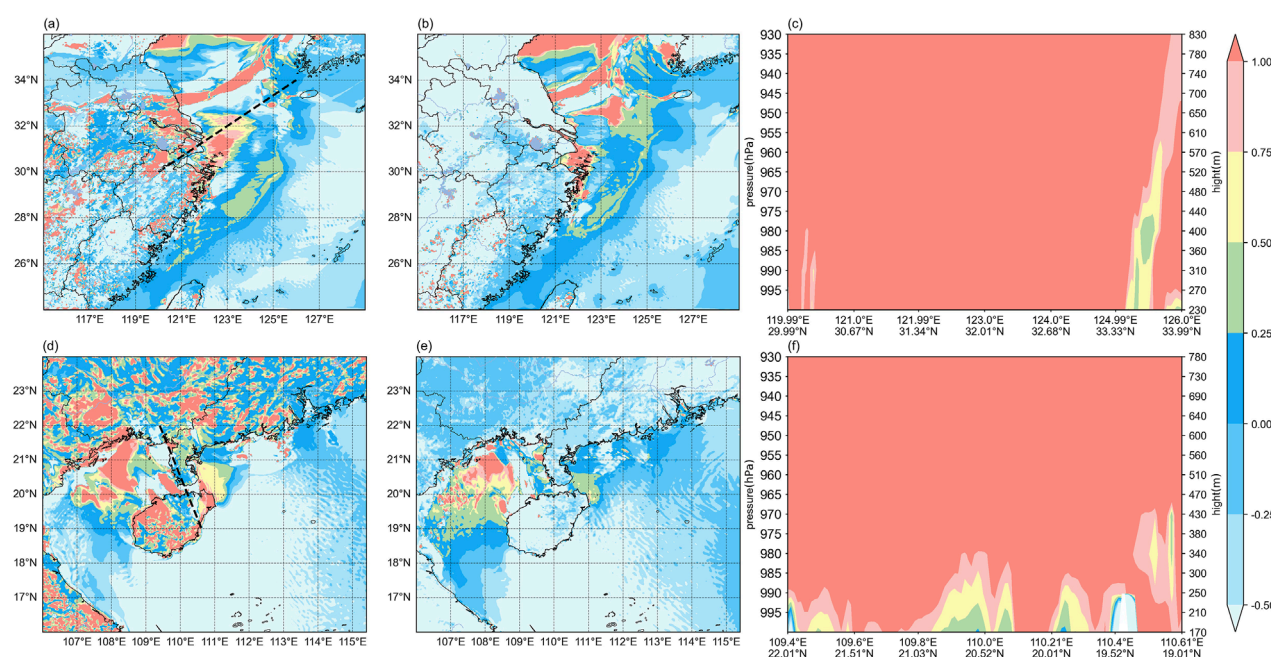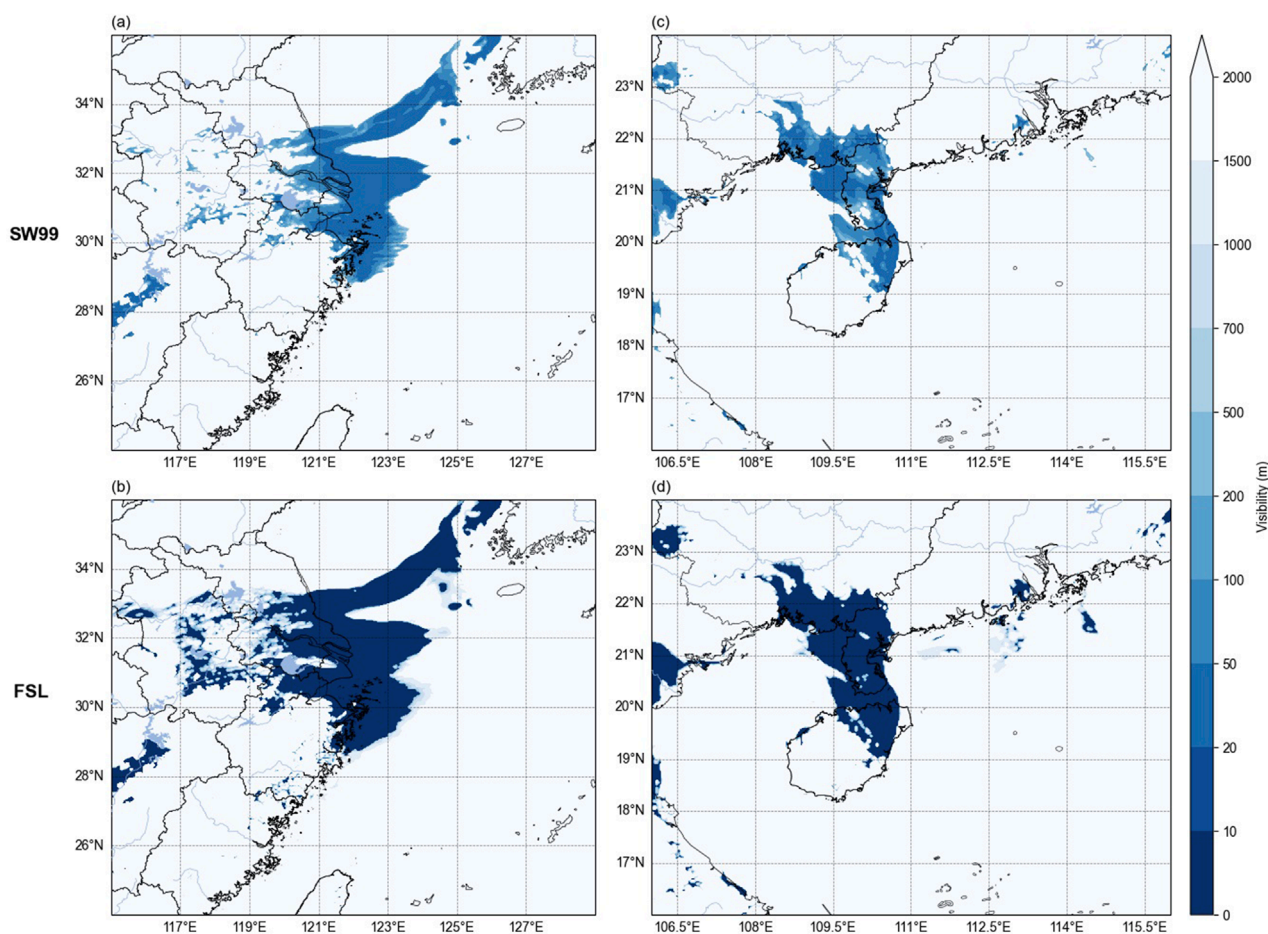

FIGURE 11
Richardson number distributions for Zhejiang case (the top panel) at **(a)** 0000 UTC, **(b)** 0600 UTC, and **(c)** the cross section at 0000 UTC on 30 March, 2018; and for Qiongzhou Strait case (the bottom panel) at **(d)** 0000 UTC, **(e)** 0600 UTC, and **(f)** the cross section at 0000 UTC on 24 January, 2021.

threshold (Equation 1). Due to the complexity of the boundary layer and microphysical processes, the forecast error of liquid water content in numerical models is much larger than that for other conventional meteorological parameters, which leads to a larger error in visibility prediction. The FSL calculation formula is simpler, but its results are highly sensitive to relative humidity (Equation 2). In regions with lower relative humidity, the calculated visibility is very small, while in areas with 100% relative humidity, the visibility value is zero, leading to a concentration of low visibility values in the fog area.

FIGURE 12
Visibility distributions calculated by the SW99 and FSL formulas (Unit: m) for Zhejiang case (the left column) with **(a)** SW99 algorithm, **(b)** FSL algorithm at 0000UTC on 30 March, 2018; for Qiongzhou Strait case (the right column) with **(c)** SW99 algorithm, **(d)** FSL algorithm at 0000UTC on 24 January, 2021.

To compare the FSL algorithm and the SW99 algorithm in fog forecasting, the Fraction Skill Score (FSS) and the Equitable Threat Score (ETS) were used to evaluate the visibility prediction results of four experiments (Figure 13). The evaluation was based on three visibility thresholds: 10 km, 1 km, and 2 km. The results show that when the visibility threshold is set to 10 km (with CMA defining visibility below 10 km as light fog), both the FSS and ETS of the FSL algorithm are higher than those of the SW99 algorithm, indicating that the FSL algorithm performs better in predicting the spatial distribution of fog (i.e., the distribution of fog areas). Specifically, the FSL algorithm seems to more accurately identify areas with visibility below 10 km, and the spatial consistency of these areas' predictions with actual observations is stronger. However, when the visibility threshold is set to 1 km, the FSS and ETS of the FSL algorithm are both lower than those of the SW99 algorithm, indicating that the FSL algorithm fails to effectively capture the details and local features of the fog under lower visibility thresholds. The SW99 algorithm may have higher precision and adaptability in this kind of low visibility situation. The results (Figures 12, 13) show that FSL has higher accuracy in forecasting the fog area range compared to SW99, but its ability to predict fog visibility values still needs improvement.

6 Summary and discussion

Based on two persistent sea fog events, one along the Zhejiang coastline in March 2018 and the other in the Qiongzhou Strait in January 2021, this study combines diagnostic analysis with numerical modeling to explore the formation mechanisms of advection-cooled sea fog. In addition, the visibility prediction methods are also compared with different model parameter factors.

It is found that the persistent sea fogs in Zhejiang and Qiongzhou Strait exhibit significant differences in their thermodynamic-dynamic coupling mechanisms and vertical structures. The Zhejiang case is dominated by warm, moist advection fog, with thermodynamic conditions characterized by low sea surface temperature and a large sea-air temperature gradient. Additionally, the relative humidity near the surface is ≥ 90%, turbulence is significantly suppressed in the fog area, and the inversion layer is relatively low (below approximately 850 hPa), with moderate stability. The high Richardson number (Ri) region along the Zhejiang coastline, combined with a stable high-pressure system, favors the prolonged persistence of sea fog. In contrast, in the Qiongzhou Strait case, during the advection fog stage, there is a
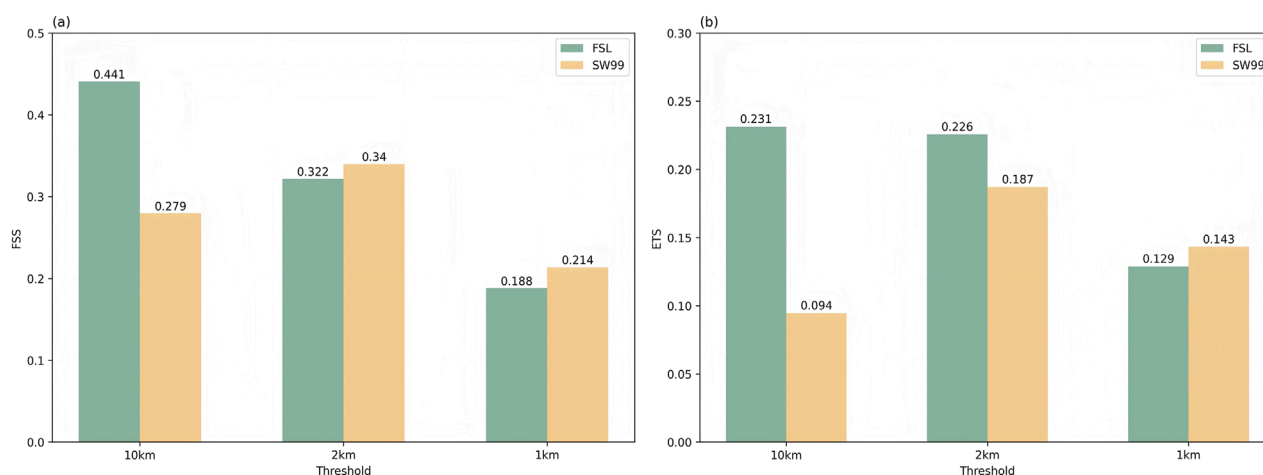
FIGURE 13
The **(a)** FSS and **(b)** ETS of visibility calculated by FSL algorithm and SW99 algorithm at 0000UTC on 30 March, 2018 and at 0000UTC on 24 January, 2021.

persistent warm advection below 950 hPa, while above 950 hPa, an inversion layer is discontinuous. The stable stratification is deeper and more thermally stable. The high Ri region in Qiongzhou Strait, due to weak turbulence, does not form thick advection fog, and turbulence is not the dominant mechanism in this case.

In the comparison of the FSL and SW99 algorithms, the fog area predicted by the SW99 algorithm is smaller, while FSL has a higher accuracy in predicting the fog area. However, its ability to predict the specific visibility values of the fog area still requires improvement.

The comparison of these two cases reveals the response characteristics of sea fog under different climatic backgrounds and provides a theoretical basis for thermodynamic-dynamic collaborative diagnosis in regional fog forecasting. This study has yet to propose a more accurate visibility calculation method based on the two visibility algorithms, and there are still some limitations. Based on the existing research, the next step will focus on exploring the integration of the strengths of the FSL and SW99 algorithms and establishing a dynamic weight distribution mechanism to optimize the visibility calculation model. By incorporating multi-source observational data (such as satellite retrieval and microwave radiometers) to refine the constraints on microphysical parameters of the fog area, and through verification with multiple weather system cases and long-term statistical tests, the collaborative forecasting accuracy of fog area and visibility under complex meteorological conditions will be improved.

Data availability statement

The original contributions presented in the study are included in the article/supplementary material, further inquiries can be directed to the corresponding author.

Author contributions

X-YY: Data curation, Formal Analysis, Resources, Visualization, Writing – original draft. F-FS: Methodology, Writing – review and

editing. H-YF: Conceptualization, Data curation, Formal Analysis, Writing – review and editing. Q-LS: Formal Analysis, Validation, Visualization, Writing – review and editing. A-QS: Conceptualization, Writing – review and editing, Investigation, Methodology, Validation. SW: Writing – review and editing, Conceptualization, Formal Analysis. HC: Investigation, Writing – review and editing, Software.

Conflict of interest

The authors declare that the research was conducted in the absence of any commercial or financial relationships that could be construed as a potential conflict of interest.

Generative AI statement

The author(s) declare that no Generative AI was used in the creation of this manuscript.

Publisher's note

References

Bang, C.-H., Lee, J., and Hong, S.-Y. (2008). Predictability experiments of fog and visibility in local airports over Korea using the WRF model. *J. Korean Soc. Atmos. Environ.* 24, 92–101.

Bergot, T., and Koracin, D. (2021). Observation, simulation and predictability of fog: review and perspectives. *Atmosphere* 12 (2), 235. doi:10.3390/atmos12020235

Cao, Z., Liu, F., He, Q., Ma, E., Li, F., and Li, B. (2022). Analysis of a continuous sea fog process along the Coast of Zhejiang in the spring of 2018. *Mar. Forecast* 39 (6), 74–82. (in Chinese).

Chen, S. H., and Sun, W. Y. (2002). A one-dimensional time dependent cloud model. *J. Meteorological Soc. Jpn.* 80 (1), 99–118. doi:10.2151/jmsj.80.99

Dudhia, J. (1989). Numerical study of convection observed during the winter monsoon experiment using a mesoscale two-dimensional model. *Atmos. Sci.* 46 (20), 3077–3107. doi:10.1175/1520-0469(1989)046<3077:nsocod>2.0.co;2

Gao, X., Gao, S., Li, Z., and Wang, Y. (2023). A revised method with a temperature constraint for assimilating satellite-derived humidity in forecasting sea fog over the yellow sea. *Front. Earth Sci.* 10, 992246. doi:10.3389/feart.2022.992246

Gultepe, I., Milbrandt, J., and Zhou, B. (2017). Marine fog: a review on microphysics and visibility prediction. *arXiv*, 345–394. doi:10.1007/978-3-319-45229-6_7

Gultepe, I., Müller, M. D., and Boybeyi, Z. (2006). A new visibility parameterization for warm-fog applications in numerical weather prediction models. *J. Appl. Meteorology Climatol.* 45, 1469–1480. doi:10.1175/JAM2423.1

Guo, J., Xu, J., and Xu, X. (2021). An observational and modeling study of a sea fog event over the yellow and east China seas on 17 march 2014. *Trop. Cyclone Res. Rev.* 10 (3), 182–190. doi:10.1016/j.tcrr.2021.09.001

Han, L., Long, J., Xu, F., and Xu, J. (2022). Decadal shift in sea fog frequency over the northern South China Sea in spring: interdecadal variation and impact of the Pacific decadal oscillation. *Atmos. Res.* 265, 105905. doi:10.1016/j.atmosres.2021.105905

Han, L., Zhang, S., Xu, F., Lü, J., Lu, Z., Ye, G., et al. (2022). Simulations of sea fog case impacted by air–sea interaction over South China Sea. *Front. Mar. Sci.* 9, 1000051. doi:10.3389/fmars.2022.1000051

He, J., Ren, X., Wang, H., Shi, Z., Zhang, F., Hu, L., et al. (2022). Analysis of the microphysical structure and evolution characteristics of a typical sea fog weather event in the eastern sea of China. *Remote Sens.* 14 (21), 5604. doi:10.3390/rs14215604

Hong, Y. S., Noh, Y., and Dudhia, J. (2006). A new vertical diffusion package with an explicit treatment of entrainment processes. *Am. Meteorological Soc.* 134 (9), 2318–2341. doi:10.1175/mwr3199.1

Huang, H., Liu, H., Huang, J., Mao, W., and Bi, X. (2015). Atmospheric boundary layer structure and turbulence during sea fog on the southern China Coast. *Mon. Weather Rev.* 143 (5), 1907–1923. doi:10.1175/MWR-D-14-00207.1

Hwang, S.-H., Park, S. K., Park, S. H., and Kwon, K. W. (2023). RDCP: a real time sea fog intensity and visibility estimation algorithm. *J. Mar. Sci. Eng.* 12 (1), 53. doi:10.3390/jmse12010053

Jiménez, P. A., Dudhia, J., González, R. J. F., Navarro, J., Montávez, J. P., and García-Bustamante, E. (2012). A revised scheme for the WRF surface layer formulation. *Mon. Weather Rev.* 140 (3), 898–918. doi:10.1175/mwr-d-11-00056.1

Kain, J. S. (2004). The kain-fritsch convective parameterization: an update. *Am. Meteorological Soc.* 43 (1), 170–181. doi:10.1175/1520-0450(2004)043<0170:tkcpau>2.0.co;2

Kim, S., Moon, J.-H., and Kim, T. (2021). A coupled numerical modeling study of a sea fog case after the passage of typhoon muifa over the yellow sea in 2011. *J. Geophys. Res. Atmos.* 126, e2020JD033875. doi:10.1029/2020JD033875

Koračin, D., Lewis, J., Thompson, W. T., Dorman, C. E., and Businger, J. A. (2001). Transition of stratus into fog along the California Coast: observations and modeling. *J. Atmos. Sci.* 58 (13), 1714–1731. doi:10.1175/1520-0469(2001)058<1714:TOSIFA>2.0.CO;2

Kunkel, B. A. (1984). Parameterization of droplet terminal velocity and extinction coefficient in fog models. *Clim. Appl. Meteorology* 23 (01), 34–41. doi:10.1175/1520-0450(1984)023<0034:podtva>2.0.co;2

Lee, E., Kim, J. H., Heo, K. Y., and Cho, Y. K. (2021). Advection fog over the eastern yellow sea: WRF simulation and its verification by satellite and *in situ* observations. *Remote Sens.* 13 (8), 1480. doi:10.3390/rs13081480

Lewis, J. M., Koračin, D., and Redmond, K. T. (2004). Sea fog research in the United Kingdom and United States: a historical essay including outlook. *Bull. Am. Meteorological Soc.* 85 (3), 395–408. doi:10.1175/BAMS-85-3-395

Li, Y., Li, M. Y., Liu, S. X., Shi, X., Li, K. F., and Bendix, J. (2023). Detection of dawn sea fog/low stratus using geostationary satellite imagery. *Remote Sens. Environ.* 294, 113622. doi:10.1016/j.rse.2023.113622

Liang, A., Zhang, Q., Liu, K., and Shen, H. (2009). The 3D-Var data assimilation experiments on a dense fog event over the central plain of China. *Meteorological Res.* 23 (1), 116–127.

Liang, J., and Griswold, J. D. S. (2024). Characteristics of yellow sea fog under the influence of eastern China aerosol plumes. *Remote Sens.* 16 (13), 2262. doi:10.3390/rs16132262

Meng, L., Liu, L., and Tian, M. (2025). Numeral simulation of impacts of sea land breeze on the formation and dissipation of the bohai sea fog. *Atmos. Res.* 323, 108190. doi:10.1016/j.atmosres.2025.108190

Mlawer, E. J., Taubman, S. J., Brown, P. D., Iacono, M. J., and Clough, S. A. (1997). Radiative transfer for inhomogeneous atmospheres: RRTM, a validated correlated-k model for the longwave. *J. Geophys. Res. Atmos.* 102 (D14), 16663–16682. doi:10.1029/97JD00237

Niu, F., Li, Z., Li, C., Lee, K.-H., and Wang, M. (2010). Increase of wintertime fog in China: potential impacts of weakening of the eastern Asian monsoon circulation and increasing aerosol loading. *J. Geophys. Res. Atmos.* 115, D21214. doi:10.1029/2009JD013484

Niu, S., Lu, C., Yu, H., Zhao, L., and Lü, J. (2010). Fog research in China: an overview. *Adv. Atmos. Sci.* 27 (3), 639–662. doi:10.1007/s00376-009-8174-8

Pahlavan, R., Moradi, M., Tajbakhsh, S., Azadi, M., and Rahnama, M. (2021). Fog probabilistic forecasting using an ensemble prediction system at six airports in Iran for 10 fog events. *Meteorol. Appl.* 28 (6), e2033. doi:10.1002/met.2033

Ryu, H.-S., and Hong, S. (2020). Sea fog detection based on normalized difference snow index using advanced himawari imager observations. *Remote Sens.* 12 (9), 1521. doi:10.3390/rs12091521

Sim, S., Im, J., Jung, S., and Han, D. (2024). Improving short-term prediction of ocean fog using numerical weather forecasts and geostationary satellite-derived ocean fog data based on AutoML. *Remote Sens.* 16 (13), 2348. doi:10.3390/rs16132348

Tian, M., Wu, B., Huang, H., Zhang, H., Zhang, W., and Wang, Z. (2019). Impact of water vapor transfer on a circum-bohai-sea heavy fog: observation and numerical simulation. *Atmos. Res.* 229, 1–22. doi:10.1016/j.atmosres.2019.06.008

Wang, Y., Qiu, Z. F., Zhao, D. Z., Ali, M. A., Hu, C., Zhang, Y., et al. (2023). Automatic detection of daytime sea fog based on supervised classification techniques for FY-3D satellite. *Remote Sens.* 15 (9), 2283. doi:10.3390/rs15092283

Wang, Y. M., Gao, S. H., Fu, G., Sun, J., and Zhang, S. (2014). Assimilating MTSAT-derived humidity in nowcasting sea fog over the yellow sea. *Weather Forecast.* 29 (2), 205–225. doi:10.1175/waf-d-12-00123.1

Xu, D., Chen, H., Chen, Y., Liu, D., Ge, F., Ye, X., et al. (2025). The impact of assimilating FY-3D microwave humidity sounder II radiance data on the analysis and forecast of two advection fog cases. *Atmos. Res.* 323, 108162. doi:10.1016/j.atmosres.2025.108162

Yang, L., Ding, S., Liu, J.-W., and Zhang, S.-P. (2024). Effects of radiative cooling on advection fog over the northwest Pacific Ocean: observations and large-eddy simulations. *Atmos. Chem. Phys.* 24, 6809–6824. doi:10.5194/acp-24-6809-2024

Yang, Y., and Gao, S. (2019). The impact of turbulent diffusion driven by fog-top cooling on sea fog development. *J. Geophys. Res. Atmos.* 124 (24), 14059–14072. doi:10.1029/2019JD031562

Yang, Z. L., Niu, G. Y., Mitchell, K. E., Chen, F., Ek, M. B., Barlage, M., et al. (2011). The community noah land surface model with multiparameterization options (Noah-MP): 2. Evaluation over global river basins. *J. Geophys. Res.* 116 (D12), D12110. doi:10.1029/2010jd015140

Yun, J., and Ha, K.-J. (2022). Physical processes in sea fog formation and characteristics of turbulent air-sea fluxes at socheongcho ocean research station in the yellow sea. *Front. Mar. Sci.* 9, 825973. doi:10.3389/fmars.2022.825973

Zhang, S.-P., Xie, S. P., Liu, Q. Y., Yang, Y. Q., Wang, X. G., and Ren, Z. P. (2009). Seasonal variations of yellow sea fog: observations and mechanisms. *J. Clim.* 22 (24), 6758–6772. doi:10.1175/2009JCLI2806.1